

# Boosting the Stability of Highly Flexible Cathodes in Zinc-Ion Batteries via the Pillaring Effect of Molybdenum in $\alpha\text{-MnO}_2$

Yujin Ren,<sup>[a]</sup> Siwen Zhang,<sup>\*[a]</sup> Bosi Yin,<sup>[a]</sup> Jiong Rui Loh,<sup>[c]</sup> Yaxi Ding,<sup>[a]</sup> Xinjun Huang,<sup>[a]</sup> Jiazhuo Li,<sup>[a]</sup> Hui Li,<sup>[b]</sup> and Tianyi Ma<sup>\*[b]</sup>

Flexible zinc-ion batteries (ZIBs) have been developed by leaps and bounds in recent years. As an important cathode material, the stability of manganese dioxide is crucial to the service life and mechanical endurance of the batteries. Herein, we report the feasibility of using a molybdenum-doped  $\alpha\text{-MnO}_2$  (MMO) grown on carbon cloth (CC) as a flexible cathode. For CC@MMO electrodes, first, the pillaring effect of the Mo atoms can stabilize the tunnel structure and reduce the energy barrier of  $\text{Zn}^{2+}$  migration. The battery has 80% capacity retention after 1392 cycles at 0.5  $\text{A g}^{-1}$ , which is leading the current study. Then, the electrodes exhibit a unique array

structure on the microscopic level, in which independently grown nanowires help buffer external stresses and improve the flexibility and stability of the electrodes. The discharge capacity of the assembled flexible battery is maintained at an average of more than 98.3% of the initial capacity at 2.5  $\text{mA cm}^{-2}$  under different bending angles. And the microstructure of the electrodes is well maintained after 50 times of repeated bending. This work thus presents a flexible cathode with remarkable stability and survivability, which seeks to supplement the present development of advanced energy storage devices.

## Introduction

With growing strides towards new energy systems, the development of new energy storage devices is salient for newfound applications and environmental sustainability.<sup>[1,2]</sup> Being widely used in storage and transmission in smart electronics, much work has been conducted to develop advanced energy storage devices to be flexible, lightweight, robust and wearable.<sup>[3,4]</sup> Although flexible lithium-ion batteries have high energy densities, the inherent flammability and toxicity of organic electrolytes used present safety risks when bent or under harsh conditions, limiting practical

applicability.<sup>[5,6]</sup> Therefore, it is crucial to explore safer battery systems that are safe for use, even when folded or twisted. One such candidate is flexible aqueous ZIBs, which are competitive green power sources with excellent safety, high theoretical capacity (820  $\text{mAh g}^{-1}$ ), low cost and high electrolyte conductivity.<sup>[7,8]</sup> However, to further optimize the performance of flexible ZIBs, improving innovative flexible cathodes should be a focus since it directly affects the capacity and cycle stability of the battery.<sup>[9]</sup>

Generally, manganese-based materials, vanadium-based materials, Prussian blue analogues and organic polymers are often used as cathode materials for flexible ZIBs. In particular,  $\text{MnO}_2$  has played a great role in the research of ZIBs by virtue of its environmental friendliness, low cost, large specific capacity and high operating voltage as well as its crystal structure.<sup>[10-12]</sup> However, during the charging and discharging process,  $\text{MnO}_2$  often suffers from severe material dissolution and structural collapse, which can shorten the service life of the battery and reduce its energy storage capacity. Therefore, nanostructure design, carbon material coating and doping are often used to improve the electrochemical properties of  $\text{MnO}_2$  cathodes. For example, Islam et al. used carbon-coated  $\alpha\text{-MnO}_2$  to improve the electrical conductivity of the material and inhibit the dissolution of  $\text{MnO}_2$ , extending the cycle life of the electrode.<sup>[13]</sup> However, carbon coating will reduce the active specific surface area of the material and hinder ion diffusion, which is not conducive to reflecting the rate capability of the electrode. Coincidentally, Luo et al. designed hierarchically interconnected  $\text{MnO}_x@\text{Ti}_3\text{C}_2\text{T}_x$  materials at the nanoscale, with electrodes having a parallel microstructure and exhibiting extremely excellent rate performance.<sup>[14]</sup> Nevertheless, the sophisticated structural design often increases the difficulty of

- [a] Y. Ren, Dr. S. Zhang, Prof. B. Yin, Y. Ding, Dr. X. Huang, J. Li  
 Institute of Clean Energy Chemistry  
 Key Laboratory for Green Synthesis and Preparative Chemistry of Advanced Material  
 College of Chemistry  
 Liaoning University  
 Shenyang 110036 (P. R. China)  
 E-mail: zhangsiwen@lnu.edu.cn
- [b] Dr. H. Li, Prof. T. Ma  
 School of Science, RMIT University  
 Melbourne, VIC 3000 (Australia)  
 E-mail: tianyi.ma@rmit.edu.au
- [c] J. R. Loh  
 Department of Materials Science and Engineering  
 National University of Singapore  
 117575 (Singapore)

 Supporting information for this article is available on the WWW under <https://doi.org/10.1002/batt.202300132>

 An invited contribution to a Special Collection on Young Scientists in Battery Research

 © 2023 The Authors. *Batteries & Supercaps* published by Wiley-VCH GmbH. This is an open access article under the terms of the Creative Commons Attribution License, which permits use, distribution and reproduction in any medium, provided the original work is properly cited.

synthesizing the material, hindering practical applicability. Yadav et al. embedded Cu into the cathode of layered  $\text{MnO}_2$  by simple solution mixing and later used the redox potential of Cu to reversibly engage in charge storage, ultimately achieving a substantial increase in electrode cycle life and energy density.<sup>[15]</sup> Park et al. prepared a low-cost and high-capacity cathode material by introducing Mo into the nickel-rich layer cathode.<sup>[16]</sup> Elemental doping is economical and effective in improving material properties compared to other modification strategies. Among various elements, low-valent metallic elements such as  $\text{Na}^+$  and  $\text{Ca}^{2+}$ , although they can expand the layer spacing or reduce electrostatic repulsion, their valence states are immutable and cannot provide additional capacity for the reaction.<sup>[17]</sup> In contrast, after Mo atoms are doped into  $\text{MnO}_2$ , in addition to stabilizing the lattice structure, inhibiting material dissolution and enhancing material conductivity, the stable and abundant valence state of Mo element can make multivalent leaps during electrochemical reactions, thus contributing additional capacity to the system.<sup>[10,18]</sup> Moreover, the high valence Mo can induce the two-electron reaction of  $\text{MnO}_2$ , which can greatly enhance the energy density of the battery.<sup>[19]</sup> Finally, Mo doping also has outstanding advantages in stabilizing lattice oxygen and improving the microscopic morphology of the material.<sup>[20,21]</sup> In addition, metals used as current collectors are prone to irreversible deformation when bent, and its substantial mass can reduce the energy density of the battery. In contrast, CC has excellent flexibility and electrical conductivity, as well as high tensile strength, making it a stable and reliable current collector.<sup>[22]</sup>

Herein, we report a flexible cathode with long cycle life and excellent electrochemical stability. Molybdenum-incorporated  $\text{MnO}_2$  was grown on a CC substrate by a simple one-step hydrothermal method to prepare the CC@MMO electrode. The cathode has a regular nanowire array, which can shorten the ion transport path in the reaction process. *Ex-situ* measurements demonstrate that it is the co-insertion of  $\text{Zn}^{2+}$  and  $\text{H}^+$  that participated in the redox reaction of the electrode. Climbing Image-Nudged Elastic Band (CI-NEB) DFT calculation verifies that the introduction of Mo produces a pillar effect that stabilizes the tunneling structure and effectively reduces the migration potential of zinc ions in the lattice. The Zn//CC@MMO retains 80% capacity after 1392 cycles at a low current density of  $0.5 \text{ A g}^{-1}$ . At the current density of  $2.5 \text{ mA cm}^{-2}$ , the capacity retention of the prepared flexible battery can reach 98.3% when bent at different angles. Additionally, the battery demonstrated excellent stability as it was capable of powering electronics even when folded, struck and after being sheared. Hence, this work seeks to showcase the feasibility of this material for use as an advanced flexible cathode.

## Result and Discussion

The schematic fabrication process for the CC@MMO nanowires is depicted in Figure 1(a). The MMO was uniformly grown on CC by a facile one-step hydrothermal method to prepare a

mechanically flexible cathode. The microscopic morphology of the CC@MMO electrode can be seen by scanning electron microscopy (SEM) image in Figure 1(b), where the MMO shows an overall regular array of nanowires and is arranged in an ordered and oriented manner on the CC fibers. As shown in Figure 1(c), the interconnection of nanowires facilitates the internal conduction of electrons and the presence of voids inside the array can facilitate the transport of ions.<sup>[23]</sup> In contrast, the microstructure of the CC@ $\text{MnO}_2$  electrode exhibits a tightly wound state (Figure S1a), and it is further evident from Figure S1(b) that the  $\text{MnO}_2$  nanowires grow in a more disordered manner and tend to form large stacks. The energy-dispersive X-ray spectroscopy (EDS) images show a homogeneous distribution of the Mo,

Mn, C and O elements in the CC@MMO sample (Figure 1d). Similarly, in the CC@ $\text{MnO}_2$  electrode, the element distribution is uniform (Figure S2). Further investigation of the internal microstructure of the materials through transmission electron microscopy (TEM) images shows that the single nanowires in the two samples are similar in shape and both have large aspect ratios (Figures 1e, S3). According to high-resolution TEM image in Figure S4(a), the CC@ $\text{MnO}_2$  materials have a continuous distribution of crystal planes and well-arranged lattice fringes. And the insets show that the d-spacings between the planes are 0.19 and 0.24 nm, corresponding to the (510) and (400) planes of tetragonal phase  $\alpha\text{-MnO}_2$  (JCPDS No. 44-0141), respectively.<sup>[24]</sup> In contrast, the CC@MMO materials exhibit disordered lattice orientations (Figure 1f), and these faint or missing lattice stripes are indicative of the low crystallinity of the active materials and the presence of lattice defects.<sup>[25,26]</sup> This structure can provide additional electroactive sites and lower the potential barrier, facilitating the diffusion of zinc ions.<sup>[27,28]</sup> Moreover, the illustrations show that the interplanar d-spacings of the compound are 0.17 and 0.20 nm, corresponding in turn to the (440) and (321) planes of  $\alpha\text{-MnO}_2$ . The crystalline structure of the two composites was further determined by selected area electron diffraction (SAED) patterns. The diffraction spots on the (510) and (400) planes in CC@ $\text{MnO}_2$  (Figure S4b) and on the (321), (402), (411) and (420) planes in CC@MMO (Figure 1g) are both indexed to the tetragonal structure of manganese dioxide. Meanwhile, inductively coupled plasma emission spectrometry (ICP-OES) measurement explored the content of Mn and Mo elements in MMO, and the percentage of Mo was 0.15% (Table S1).

The X-ray diffraction (XRD) results further illustrate the consistency and differences between the two samples before and after incorporation in terms of the phase composition and the crystal structure. According to the information in Figure 2(a), the CC@MMO and CC@ $\text{MnO}_2$  have similar XRD patterns, where the characteristic peak located at  $26^\circ$  is from carbon cloth (JCPDS No. 75-1621) and points to the (002) crystal plane.<sup>[29,30]</sup> The remaining diffraction peaks can be accurately indexed to the tetragonal phase of  $\alpha\text{-MnO}_2$  (JCPDS No. 44-0141).<sup>[31]</sup> As shown in Figure 2(b), the Mo atom replaces the Mn atom in the original  $\alpha\text{-MnO}_2$  lattice, and the MMO crystal consists of the classical  $[\text{MnO}_6]$  octahedral unit, forming a [2\*2] and [1\*1] tunnel structure with corner-shared

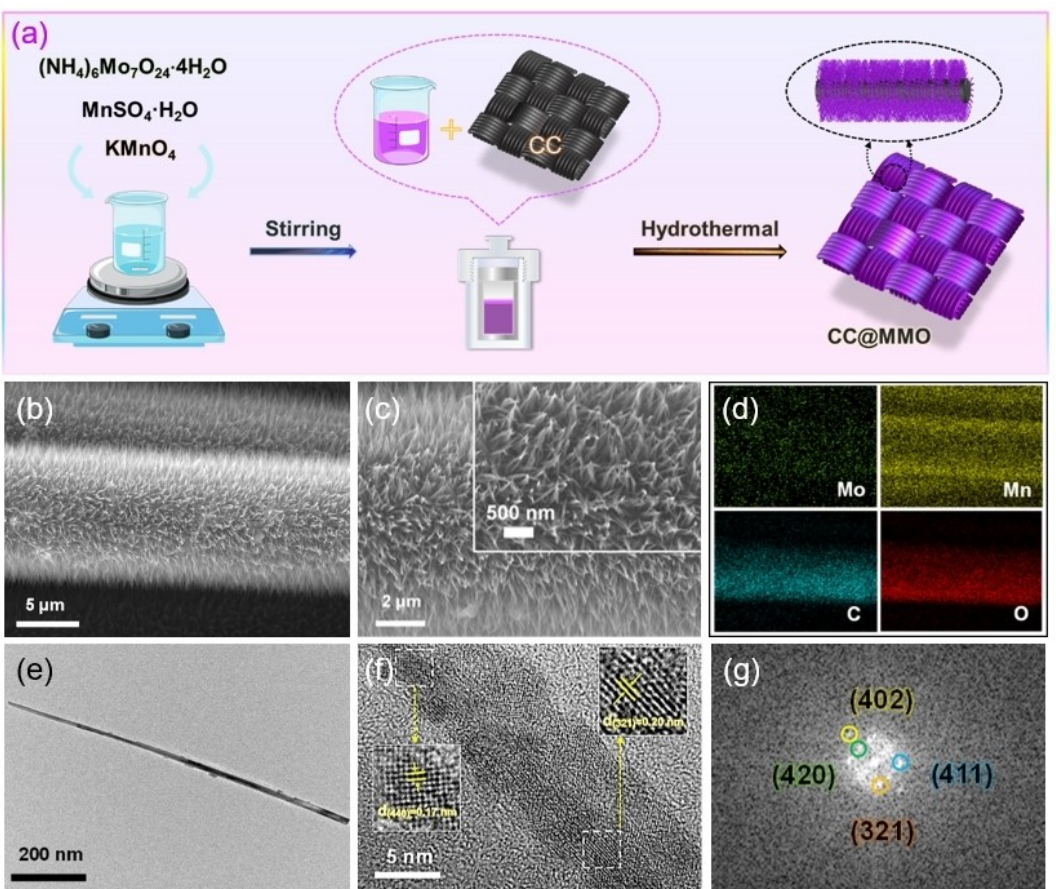


**Figure 1.** a) Schematic diagram of the synthesis process for CC@MMO. b), c) SEM images of CC@MMO. d) EDS mapping images of CC@MMO. e) TEM and f) high-resolution TEM images of the CC@MMO. g) The corresponding SAED pattern of CC@MMO.

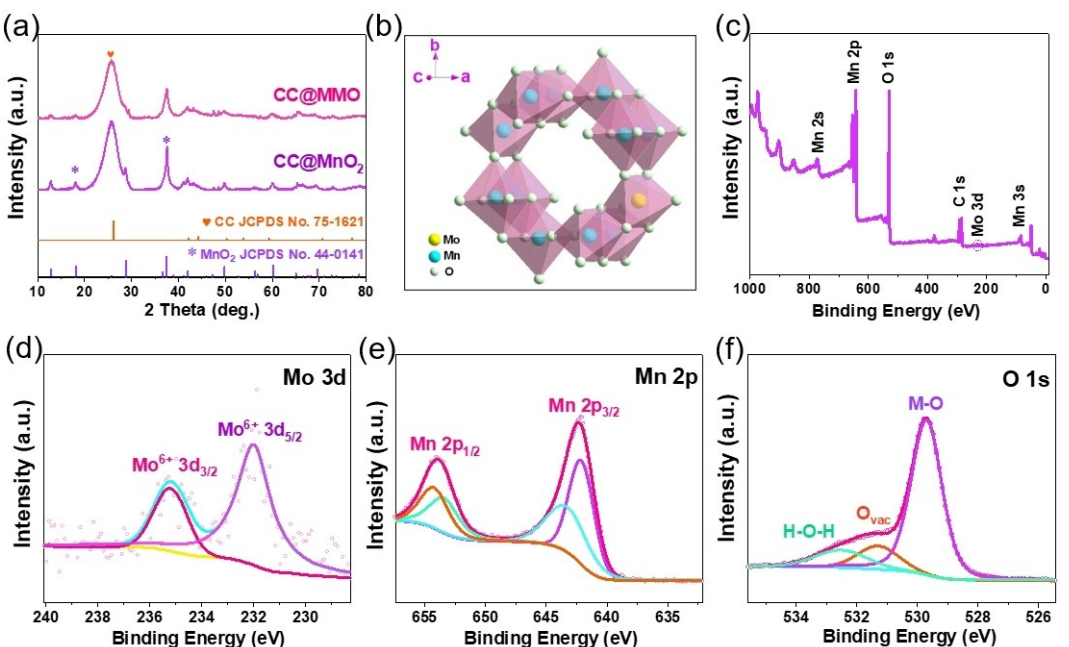


**Figure 2.** a) XRD patterns of CC@MMO and CC@ $\text{MnO}_2$ . b) Structural illustration of MMO. c) Full XPS spectra of CC@MMO. High-resolution XPS spectrum of CC@MMO. d) Mo 3d. e) Mn 2p. f) O1s.

connection.<sup>[32,33]</sup> Specifically, by comparing the diffraction peaks at 37.5° (Figure S5), it is found that the CC@MMO peak position has a relatively small angle due to the expansion of the tunnel space by the Mo introduced, which widens the crystalline plane spacing.<sup>[34]</sup> And the lower peak intensity of CC@MMO reveals its lower crystallinity,<sup>[35]</sup> which is consistent with the high-resolution TEM results.

To further investigate the chemical composition and bond state of the CC@MMO material, X-ray photoelectron spectroscopy (XPS) was used for characterization. The results are as follows, with XPS full spectrum (Figure 2c) demonstrating the presence of Mo, Mn, O and C elements. The high-resolution XPS spectrum of C 1s (Figure S6) shows a total of three peaks at binding energies of 284.6, 285.8, and 288.0 eV, corresponding to C–C, C–O and C=O bonds respectively.<sup>[36]</sup> In the Mo 3d spectrum (Figure 2d), the peaks at 232.0 and 235.3 eV represent the Mo 3d<sub>5/2</sub> and Mo 3d<sub>3/2</sub> orbitals of Mo<sup>6+</sup> in turn, which are associated with the formation of Mo–O bonds, indicating the successful synthesis of Mo-incorporated complexes.<sup>[20,37]</sup> The Mn 2p spectrum (Figure 2e) reveals that the Mn element comprises two valence states, Mn<sup>3+</sup>

(642.2 eV and 653.6 eV) and Mn<sup>4+</sup> (643.7 eV and 654.4 eV), with a binding energy separation of 11.6 eV between Mn 2p<sub>3/2</sub> (642.4 eV) and Mn 2p<sub>1/2</sub> (654.0 eV) orbitals.<sup>[38,39]</sup> The three split peaks in the O 1s spectra (Figure 2f) indicate metal–oxygen bond in the lattice (529.7 eV), oxygen vacancy (531.4 eV) and adsorbed water (532.5 eV).<sup>[40,41]</sup> Subsequently, Raman spectroscopy (Figure S7) indicates stretching vibrations, including the F<sub>2g</sub> vibrational mode (514 cm<sup>-1</sup>) and the A<sub>g</sub> vibrational mode (579 and 636 cm<sup>-1</sup>), as well as bending vibrations (399 cm<sup>-1</sup>) and antisymmetric stretching vibrations (739 cm<sup>-1</sup>) of Mn–O bonds in MnO<sub>6</sub> octahedra in the CC@MMO band.<sup>[42]</sup> Distinctly, in the CC@MnO<sub>2</sub> pattern, only the primary peak at 658 cm<sup>-1</sup> and two secondary peaks at 319 and 371 cm<sup>-1</sup> are attributed to the Mn–O bond.<sup>[43]</sup> This is mainly due to the fact that the introduction of molybdenum can cause changes in peak intensity and the red shift in peak position.<sup>[21,44]</sup>

Having confirmed the effective doping of molybdenum, the electrochemical properties of the electrodes were then tested. As shown in Figure 3(a), the experiment was conducted with CC@MMO and CC@MnO<sub>2</sub> with an area of 1 cm<sup>2</sup> as the cathode and matched with zinc foil as the anode, using 1 M Zn(CF<sub>3</sub>SO<sub>3</sub>)<sub>2</sub>

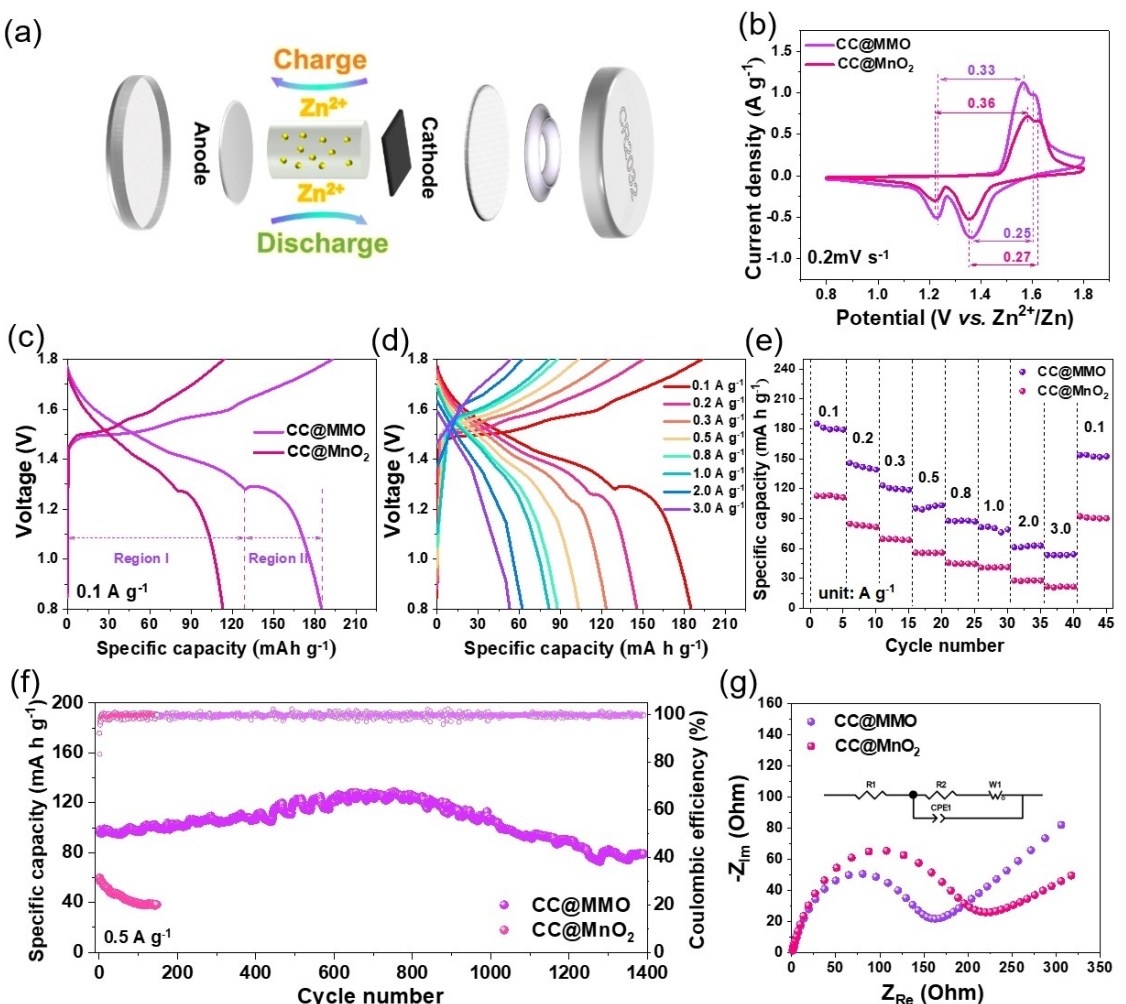


**Figure 3.** a) Schematic diagram of the structure of coin cells. b) CV curves at 0.2 mVs<sup>-1</sup> and c) GCD profiles at 0.1 Ag<sup>-1</sup> of Zn//CC@MMO and Zn//CC@MnO<sub>2</sub>. d) GCD profiles of Zn//CC@MMO with different current densities from 0.1 to 3.0 Ag<sup>-1</sup>. Electrochemical properties of Zn//CC@MMO and Zn//CC@MnO<sub>2</sub>. e) Rate performance. f) cycling durability and coulombic efficiency at 0.5 Ag<sup>-1</sup>. g) EIS spectra.

+0.1 M MnSO<sub>4</sub> aqueous solution as the electrolyte to form CR2032 type coin cells. Figure 3(b) shows the cyclic voltammetry (CV) curves for both materials at a sweep rate of 0.2 mV s<sup>-1</sup>. Similarly, the batteries exhibit two distinct pairs of redox peaks over the operating voltage range of 0.8–1.8 V. According to the previous research, the cathodic peaks formed at 1.23 and 1.36 V for  $\alpha$ -MnO<sub>2</sub> cathode materials (exemplified by CC@MMO) are due to the insertion of H<sup>+</sup> and Zn<sup>2+</sup> as well as the reduction of Mn<sup>4+</sup>, correspondingly, the anodic peaks at 1.61 and 1.56 V are due to the extraction of ions and the transition from Mn<sup>3+</sup> to Mn<sup>4+</sup>.<sup>[45,46]</sup> By contrast, the curves differ in that CC@MMO has a higher peak current density and a greater curve area, demonstrating its superior reaction kinetics and larger electrochemical capacity.<sup>[47]</sup> In addition, the voltage gaps of the CC@MMO (0.25 and 0.33 V) are smaller than that of CC@MnO<sub>2</sub> (0.27 and 0.36 V), due to the increased conductivity of the material after molybdenum doping, which eases the voltage polarization of the coin cells.<sup>[48]</sup> As shown in the galvanostatic charge-discharge (GCD) curves in Figure 3(c), the numerical difference in discharge capacity between Zn//CC@MMO and Zn//CC@MnO<sub>2</sub> is 72 mAh g<sup>-1</sup> at a current density of 0.1 A g<sup>-1</sup>, indicating a significant improvement in battery performance, which could be attributed to the more abundant reactive sites of CC@MMO. The discharge curves of the two cells have a similar shape and both have two discharge regions, noted as region I and region II. Corroborating the CV results, H<sup>+</sup> and Zn<sup>2+</sup> dominate the capacity contributions of regions I and II, respectively. When the current density increases, the discharge plateau of both batteries in region II gradually decreases or even disappears (Figures 3d, S8), this is caused by the large radius of Zn<sup>2+</sup> leading to poor kinetics of the insertion/extrusion process.<sup>[45]</sup> Figure 3(e) demonstrates the rate performance of the cells, where the discharge specific capacity of Zn//CC@MMO is significantly higher than that of Zn//CC@MnO<sub>2</sub> at different current densities, and the comparative results of the corresponding Ragone plots are shown in Figure S9.

The improved battery performance is associated with the altered lattice structure of pristine  $\alpha$ -MnO<sub>2</sub> after molybdenum was incorporated, which facilitates ion transport.<sup>[49]</sup> The results of the cycling stability, an important indicator of the performance of the battery, are presented in Figure 3(f). At a low current density of 0.5 A g<sup>-1</sup>, Zn//CC@MMO exhibited excellent cycling performance with a capacity retention of 80% after 1392 cycles, and the cell exhibited outstanding redox reversibility with the Coulombic efficiency consistently close to 100%. In addition, the discharge specific capacity increased from an initial 98.2 mAh g<sup>-1</sup> to 129.0 mAh g<sup>-1</sup> after 754 cycles, presumably due to the Mo facilitating the complete release of MnO<sub>2</sub> capacity.<sup>[19]</sup> Contrastingly, Zn//CC@MnO<sub>2</sub> exemplifies poor cycle life, with a capacity retention of only 64% after 150 cycles. Electrochemical impedance spectroscopy (EIS) test can explore the interface properties of electrode material and electrolyte, allowing a preliminary analysis of the electrochemical performance gap between the two cells. As shown in Figure 3(g), the semicircular of the Nyquist plot located in the high frequency region mirrors the electron transfer process, the intercept on the real axis represents the equivalent series resistance, which

includes the intrinsic resistance of the electrodes and electrolyte as well as the contact resistance between them, while the radius represents the charge transfer resistance ( $R_2$ ), meanwhile, the slope of the line in the low frequency is related to the solid state diffusion of ions.<sup>[50,51]</sup> According to the fitting results of the equivalent circuit in the inset, the  $R_2$  of the CC@MMO electrode is 163  $\Omega$ , which is lower than the 220  $\Omega$  of the CC@MnO<sub>2</sub> electrode, and the slope of the CC@MMO electrode is higher in the low frequency region, which proves its low diffusion resistance.

The dominant process of the reaction kinetics was investigated by CV tests to better elucidate the charge storage mechanism of the CC@MMO electrode. Figure 4(a) shows the CV curves for Zn//CC@MMO at sweep speeds of 0.2 to 1.0 mV s<sup>-1</sup>. Clearly, with the increase of the sweep rate during the discharge process, both cathode peaks show certain polarization, and the current density of peak 3 shows a significant increase, while the growth of peak 4 is blocked. According to the relationship between peak current ( $i$ ) and sweep speed ( $v$ ):<sup>[52,53]</sup>

$$i = av^b \quad (1)$$

where  $a$  and  $b$  are constants. Values of  $b$  close to 0.5 or 1 indicate a tendency for diffusion control or surface capacitance control (both double-layer capacitance and surface-confined redox reactions) of the reaction, respectively. As shown in Figure S10, the  $b$  values for peaks 1 to 3 were calculated to be between 0.5 and 0.6, indicating that diffusion control was dominant. After an approximate fit, the  $b$  value of peak 4 is less than 0.50, indicating that the solid diffusion of ions within the material is suppressed as the scan rate increases.<sup>[54,55]</sup> In addition, the ratio of the capacity contribution ( $k_1v$ ) to the diffusion contribution ( $k_2v^{1/2}$ ) was further calculated according to Equation (2).<sup>[56]</sup>

$$i = k_1v + k_2v^{1/2} \quad (2)$$

According to Figures 4(b) and S11, it can be observed that the capacitance contribution of both CC@MMO and CC@MnO<sub>2</sub> becomes larger as the sweep speed increases. The main reason for this increase is that the reaction path for ions to undergo solid-state diffusion is longer than for the surface pseudocapacitance reaction (the contribution of the double layer capacitance is almost negligible), which requires a longer diffusion time at the same scan rate. Therefore, there is a lower tendency for diffusion reactions to occur at higher scan rates, resulting in an increased contribution from pseudocapacitance and a reduction in total capacity.<sup>[57]</sup> Moreover, CC@MMO has a lower value of capacitance contribution, which indicates that the diffusion process of ions is easier after Mo doping to MnO<sub>2</sub>.

It is evident that an unhindered and stable ion diffusion pathway is essential to improve the electrochemical performance of the electrode. For this purpose, Zn<sup>2+</sup> diffusion barriers of the CC@MnO<sub>2</sub> and CC@MMO were analyzed by CI-NEB DFT calculations. Combined with Figure 4(c and d), the molybdenum atom has partially replaced the manganese atom in the

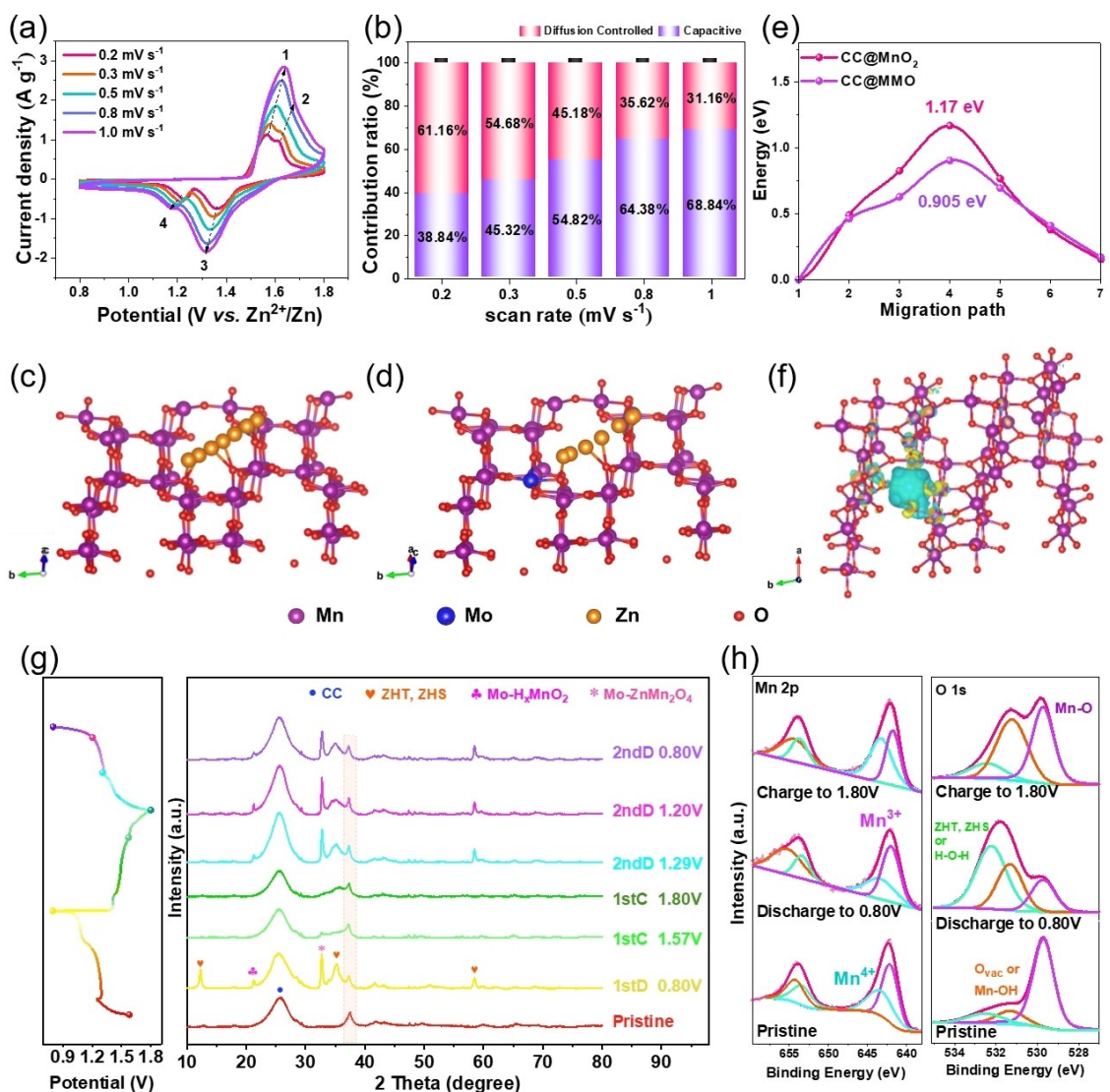


**Figure 4.** a) CV curves of the Zn//CC@MMO at different scan rates. b) Percentage of capacitance and diffusion contribution of Zn//CC@MMO. c), d) The schematic diagram of Zn<sup>2+</sup> migration in CC@MnO<sub>2</sub> and CC@MMO. e) The Zn<sup>2+</sup> diffusion barrier profiles for CC@MnO<sub>2</sub> and CC@MMO. f) Charge density difference of CC@MMO. g) Ex-situ XRD patterns of CC@MMO at different potential states. h) Ex-situ Mn 2p and O 1s XPS spectrum of the CC@MMO.

lattice. As calculated above (Figure 4e), the migration energy barriers of Zn<sup>2+</sup> on surface CC@MnO<sub>2</sub> and surface CC@MMO were 1.17 eV and 0.905 eV, respectively, indicating that the introduction of Mo atoms makes it easier for Zn<sup>2+</sup> to migrate on the Mo-incorporated MnO<sub>2</sub> surface, which is beneficial for improving the electrochemical reaction kinetics. As shown in Figure 4(f), the charge density difference of CC@MMO model indicates that there is obvious electron rearrangement and charge transfer. A stronger electronic interaction between Mo atom and MnO<sub>2</sub> was also observed, with electrons mainly transferred from MnO<sub>2</sub> to Mo atoms. The above analysis proves that the incorporation of Mo has a significant contribution to the electrode kinetics.

To further study the crystalline phase evolution and surface state changes of the CC@MMO electrode during the electrochemical reaction, ex-situ XRD and ex-situ XPS measurements were used for characterization. Ex-situ XRD patterns of the

CC@MMO cathode located at specific voltages during the first two charging and discharging processes are recorded in Figure 4(g). New diffraction peaks appear when fully discharged to 0.8 V. This is due to the embedding of H<sup>+</sup> and Zn<sup>2+</sup> to generate new phases of Mo-H<sub>x</sub>MnO<sub>2</sub> (JCPDS No. 24–0713) and Mo-ZnMn<sub>2</sub>O<sub>4</sub> (JCPDS No. 24–1133). Meanwhile, the consumption of H<sup>+</sup> increases the OH<sup>-</sup> concentration, and Zn<sup>2+</sup> combines with anions near the cathode to form zinc layered hydrates Zn<sub>5</sub>(OH)<sub>8</sub>(CF<sub>3</sub>SO<sub>3</sub>)<sub>2</sub>·0.5H<sub>2</sub>O (ZHT) and Zn<sub>4</sub>SO<sub>4</sub>(OH)<sub>6</sub>·0.5H<sub>2</sub>O (ZHS) (JCPDS No. 44–0674), which are not distinguished in this paper because of the similarity of ZHT and ZHS as previously reported.<sup>[58,59]</sup> In the process of charging to 1.8 V, these peaks gradually weaken or disappear with the removal of H<sup>+</sup> and Zn<sup>2+</sup>, and the presence of residual peaks indicates incomplete conversion, which may be the reason for the low battery capacity.<sup>[19]</sup> Overall, the characteristic peaks of the original CC@MMO are highly preserved during the two

charge-discharge processes, suggesting that the reaction process does not involve phase transition and the small peak shifts are caused by the change of the layer spacing during the ion insertion and extraction.<sup>[60]</sup> It can be concluded that the incorporation of Mo atoms stabilizes the crystal structure and thus extends the cycle life of the battery.

The results of the *ex-situ* XPS measurement are shown in Figure 4(h). The Mn 2p diagram shows that when the initial state discharge to 0.8 V, the splitting peaks of Mn<sup>3+</sup> and Mn<sup>4+</sup> both move to the lower binding energy direction, indicating that the insertion of H<sup>+</sup> and Zn<sup>2+</sup> reduces the chemical valence of Mn elements and increases the Mn<sup>3+</sup> content.<sup>[37]</sup> When charging to 1.8 V, it is obvious that the peak intensity of Mn<sup>3+</sup> decreases and the intensity of Mn<sup>4+</sup> peak increases, indicating that Mn<sup>3+</sup> is oxidized to Mn<sup>4+</sup>. For the O 1s pattern, in the complete discharged state, the intensity of the peak at 531.4 eV increases, indicating the formation of Mn–OH after the insertion of H<sup>+</sup> into the lattice. The significant increase in intensity of the peak at 532.5 eV is due to the generation of ZHT and ZHS, which simultaneously causes the peak at 529.7 eV to become lower due to their coverage of the electrode surface.<sup>[61]</sup> When charging to 1.8 V, the process is the opposite. The above analysis process corresponds to the results of XRD. Figure S12 shows the Mo 3d orbital, where the valence of Mo is always +6 during the charge and discharge process, indicating that Mo is electrochemically inactive and only serves to stabilize the lattice.<sup>[18,37]</sup> Figure S13 shows the Zn 2p pattern, after discharging to 0.8 V, two peaks with higher intensity

appear along with the insertion of Zn<sup>2+</sup>. Subsequent to charging to 1.8 V, the intensity of the peaks decreases due to the extrusion of Zn<sup>2+</sup>. The above changes are consistent with the *ex-situ* XRD results.

In order to demonstrate the value of the CC@MMO electrodes in practical application, they were assembled into flexible batteries for testing, as shown in Figure 5(a). Upon testing, the CV curves first demonstrated two pairs of redox peaks similar to those of the coin cells and maintained a well shape at different scan rates (Figure 5b), indicating a good electrochemical reaction process in the flexible ZIBs. Then, Figure 5(c) shows the discharge profiles for the battery with an area of 2 cm<sup>2</sup> at a range of current densities. The curves have two wide discharge plateaus at a low current density of 0.3 mA cm<sup>-2</sup>. Furthermore, the discharge capacities at 0.3, 0.6, 0.9, 1.5 and 2.0 mA cm<sup>-2</sup> are 0.56, 0.41, 0.32, 0.21 and 0.15 mAh cm<sup>-2</sup> respectively. Figure 5(d-f) shows the bending test of the battery at different angles. The results of the CV test at 2 mVs<sup>-1</sup> and the discharge measurement at 2.5 mA cm<sup>-2</sup> show that both the CV curves and the discharge profiles are highly consistent and almost overlap. In addition, the specific discharge capacity of the battery at 180°, 120°, 90°, 60° and 30° is 0.103, 0.101, 0.101, 0.102 and 0.101 mAh cm<sup>-2</sup>, respectively, with a high average capacity retention rate of 98.3%. To verify more visually that the doping of molybdenum atoms into the lattice has a positive effect on the macroscopic stability of the electrodes, dynamic bending tests were performed on the electrodes. The bending process is shown in Figure S14, the

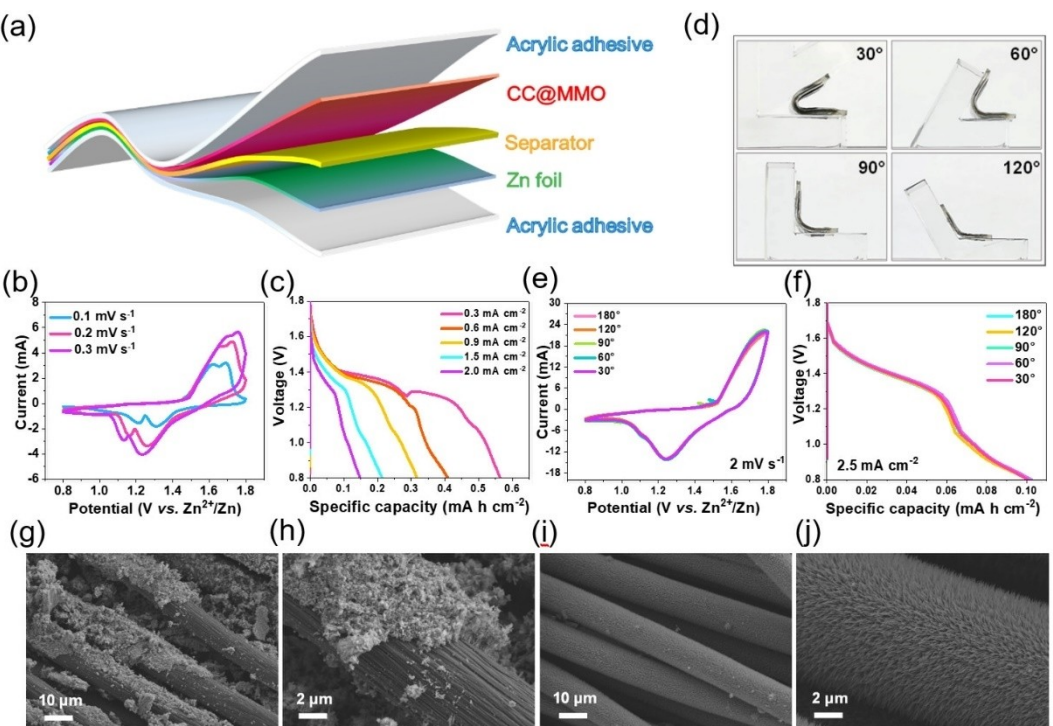


**Figure 5.** a) Structure schematic of flexible Zn//CC@MMO. Electrochemical properties of flexible Zn//CC@MMO. b) CV curves at different scan rates. c) discharge profiles at various current densities. d) Photographs of flexible Zn//CC@MMO at different bending angles. e) CV curves for different bending angles at 2 mVs<sup>-1</sup> of flexible Zn//CC@MMO. f) Discharge profiles for different bending angles at 2.5 mA cm<sup>-2</sup> of flexible Zn//CC@MMO. SEM images of g, h) CC@MnO<sub>2</sub> and i), j) CC@MMO after bending 50 times.

SEM characterization of both electrodes was performed after 50 repetitions of bending. As shown in Figure 5(g and h), the microstructure of CC@MnO<sub>2</sub> after bending showed a broken state on the whole, and a large amount of lumpy active material was detached from the CC fibers, which indicates that the electrode has low resistance to external stress and poor mechanical stability. In contrast, the original morphology of the CC@MMO cathode was well maintained after bending (Figure 5i), and the nanowire arrays were uniformly and firmly attached to the CC fibers (Figure 5j). The doping of Mo atom can stabilize the lattice structure and optimize the microscopic morphology. The independently grown nanowires can buffer the external stresses to the maximum extent, which gives the electrode excellent stability and flexibility.

Subsequently, CC@MMO was assembled into flexible batteries to explore their practical applications. A 2 cm<sup>2</sup> battery was used to power an LED light (Figure 6a) and a fan (Figure 6b) in a flat state. When folded, the battery was still able to power the LED light (Figure 6c), proving its flexibility and practicality. A 6 cm<sup>2</sup> battery was then used to illuminate the LED before and after the battery was physically knocked (Figures S15 and 6d). Thereafter, a circle with a diameter of 1.2 cm was cut out from the center of the battery. As shown in Figure 6(e and f), even after the battery is cut, it still continues to supply power to the LED and fan, demonstrating the battery has excellent resistance to external stress and outstanding durability.

## Conclusions

In summary, a method to prepare a highly stable flexible CC@MMO cathode is reported. The pillar effect of Mo enhances the stability of the tunneling structure and accelerates the carrier diffusion kinetics. During electrochemical testing, the CC@MMO cathode exhibited excellent long-cycle

stability (1392 cycles 80% retention rate) at small current densities (0.5 A g<sup>-1</sup>). When assembled into a flexible device, the battery at different bending angles had an average capacity retention of 98.3% at a current density of 2.5 mA cm<sup>-2</sup>. It also provided a stable power supply for electronics even under physical stress and after being cut. Therefore, the cathode developed has excellent structural stability and durability, and is of great practical value.

## Experimental Section

### Synthesis of materials

First, the carbon cloth (3.2 × 4 cm) was sonicated with ethanol and deionized water in turn for 30 min. Next, 0.2 g KMnO<sub>4</sub> and 0.0392 g MnSO<sub>4</sub>·H<sub>2</sub>O were dissolved with 65 ml deionized water and stirred for 5 min, and then 0.01 g (NH<sub>4</sub>)<sub>6</sub>Mo<sub>7</sub>O<sub>24</sub>·4H<sub>2</sub>O was added and stirred for 5 min. Subsequently, the above solution and treated carbon cloth were transferred to a 50 mL Teflon autoclave and reacted at 160 °C for 16 h. After cooling to room temperature, the samples were taken out and washed with ethanol and deionized water and dried under vacuum at 60 °C to obtain CC@MMO. As a control, CC@MnO<sub>2</sub> samples were prepared with the same procedure except (NH<sub>4</sub>)<sub>6</sub>Mo<sub>7</sub>O<sub>24</sub>·4H<sub>2</sub>O was not added.

### Materials characterization

The scanning electron microscopy (SEM, HITACHI, SU8010 and ZEISS Gemini 300) characterized the morphology and energy-dispersive X-ray spectroscopy (EDS) energy spectra of the samples, while transmission electron microscopy (TEM, JEM-2100) characterized the microstructure and selected area electron diffraction (SAED) patterns of the materials. Inductively coupled plasma emission spectrometry (ICP-OES, Agilent 5110) analyzed the content of metallic elements in the samples. The phase composition and valence states of the samples were analyzed by X-ray diffraction (XRD, Bruker D8-Advance) and X-ray photoelectron spectroscopy (XPS, ESCALAB 250Xi, Thermo Scientific Escalab). The

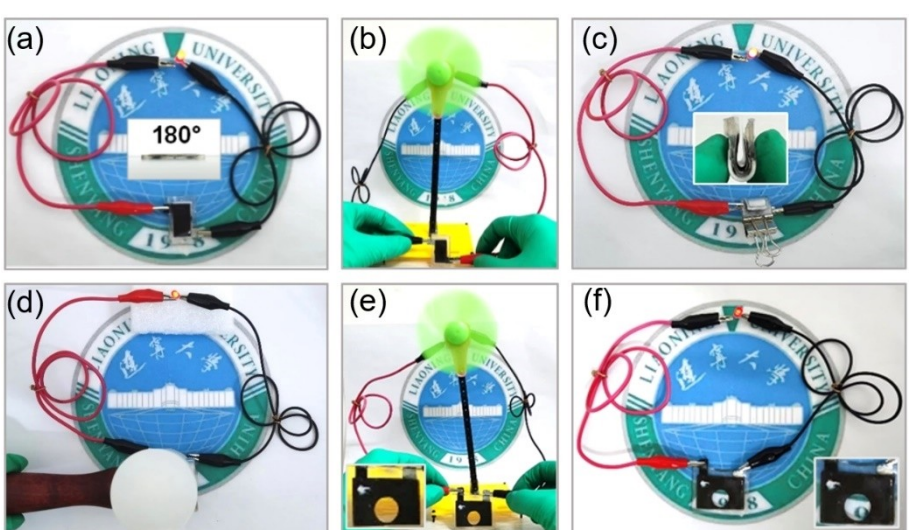


**Figure 6.** Photographs of a 2 cm<sup>2</sup> battery to power a) an LED. b) a fan and c) an LED in the folded position. d) A 6 cm<sup>2</sup> battery to power an LED in the knocked state. A 6 cm<sup>2</sup> battery to power. e) a fan and f) an LED after being cut.

bond composition of the samples was detected by Raman spectroscopy (Horiba LabRAM HR Evolution).

### Electrochemical measurements

In the CR2032 coin cell, CC@MMO or CC@ $\text{MnO}_2$  was selected as the cathode material, zinc foil as the anode, and glass fiber as the separator. The flexible battery consists of a CC@MMO cathode, a zinc foil anode and a glass fiber separator, with the outermost layer encapsulated with acrylic adhesive. All the above devices use 1 M  $\text{Zn}(\text{CF}_3\text{SO}_3)_2$  and 0.1 M  $\text{MnSO}_4$  as the electrolyte for electrochemical testing. Cyclic voltammetry (CV), electrochemical impedance spectroscopy (EIS) and galvanostatic charge-discharge (GCD) testing were completed at a multi-channel electrochemical analyzer (VMP3, Bio-Logic-Science Instruments) and NEWARE battery test system.

### Density functional theory calculations

All the DFT calculations were conducted based on the Vienna Ab-initio Simulation Package (VASP).<sup>[62,63]</sup> The exchange-correlation effects were described by the Perdew-Burke-Ernzerhof (PBE) functional within the generalized gradient approximation (GGA) method.<sup>[64,65]</sup> The core-valence interactions were accounted by the projected augmented wave (PAW) method.<sup>[66]</sup> The energy cutoff for plane wave expansions was set to 480 eV, and the  $3 \times 2 \times 1$  Monkhorst-Pack grid k-points were selected to sample the Brillouin zone integration. The vacuum space is adopted 15 Å above the surfaces to avoid periodic interactions. The structural optimization was completed for energy and force convergence set at  $1.0 \times 10^{-4}$  eV and  $0.02 \text{ eV}\text{\AA}^{-1}$ , respectively. The barriers for  $\text{Zn}^{2+}$  migration on models were calculated with the climbing-image nudged elastic band (CI-NEB) method.

### Supporting Information

Supporting Information is available from the Wiley Online Library or from the author.

### Acknowledgements

This work was supported by the National Natural Science Foundation of China (Nos. 52071171, 52202248), Liaoning BaiQianWan Talents Program (LNBQW2018B0048), Shenyang Science and Technology Project (21-108-9-04), the Research Fund for the Doctoral Program of Liaoning Province (2022-BS-114), Australian Research Council (ARC) through Future Fellowship (FT210100298, FT210100806), Discovery Project (DP220100603), Linkage Project (LP210100467, LP210200504, LP210200345, LP220100088), and Industrial Transformation Training Centre (IC180100005) schemes, CSIRO Energy Centre and Kick-Start Project, and the Australian Government through the Cooperative Research Centres Projects (CRCPXIII000077). The authors would like to thank Xiao Ming Li from SCI-GO ([www.sci-go.com](http://www.sci-go.com)) for the DFT calculation. The authors would like to thank Gao Jilong from Shiyanjia Lab ([www.shiyanjia.com](http://www.shiyanjia.com)) for the XPS analysis. Open Access publishing facilitated by RMIT University, as part of the

Wiley - RMIT University agreement via the Council of Australian University Librarians.

### Conflict of Interests

The authors declare no conflict of interest.

### Data Availability Statement

The data that support the findings of this study are available from the corresponding author upon reasonable request.

**Keywords:** flexible cathode · molybdenum · pillaring effect · zinc-ion battery

- [1] P. Ruan, S. Liang, B. Lu, H. J. Fan, J. Zhou, *Angew. Chem. Int. Ed.* **2022**, *134*, e202200598.
- [2] Y. Ding, S. Zhang, J. Li, Y. Sun, B. Yin, H. Li, Y. Ma, Z. Wang, H. Ge, D. Su, T. Ma, *Adv. Funct. Mater.* **2023**, *33*, 2210519.
- [3] C. Wang, X. Wang, C. Lin, X. S. Zhao, *Small* **2019**, *15*, 1902183.
- [4] Y. Ren, F. Meng, S. Zhang, B. Ping, H. Li, B. Yin, T. Ma, *Carbon Energy* **2022**, *4*, 446–457.
- [5] Y. Zhang, S. Deng, Y. Li, B. Liu, G. Pan, Q. Liu, X. Wang, X. Xia, J. Tu, *Energy Storage Mater.* **2020**, *29*, 52–59.
- [6] Y. Liu, A. Gao, J. Hao, X. Li, J. Ling, F. Yi, Q. Li, D. Shu, *Chem. Eng. J.* **2023**, *452*, 139605.
- [7] B.-S. Yin, S.-W. Zhang, T. Xiong, W. Shi, K. Ke, W. S. V. Lee, J. Xue, Z.-B. Wang, *New J. Chem.* **2020**, *37*, 15951–15957.
- [8] W.-J. Song, S. Lee, G. Song, H. B. Son, D.-Y. Han, I. Jeong, Y. Bang, S. Park, *Energy Storage Mater.* **2020**, *30*, 260–286.
- [9] M. Yao, Z. Yuan, S. Li, T. He, R. Wang, M. Yuan, Z. Niu, *Adv. Mater.* **2021**, *33*, 2008140.
- [10] Z. Zheng, G. Yang, J. Yao, J. Li, J. Zheng, Z. Wu, Y. Gan, C. Wang, L. Lv, H. Wan, C. Chen, H. Wang, L. Tao, J. Zhang, H. Wang, *Appl. Surf. Sci.* **2022**, *592*, 153335.
- [11] Y. Jin, L. Zou, L. Liu, M. H. Engelhard, R. L. Patel, Z. Nie, K. S. Han, Y. Shao, C. Wang, J. Zhu, H. Pan, J. Liu, *Adv. Mater.* **2019**, *31*, 1900567.
- [12] Y. Xu, G. Zhang, J. Liu, J. Zhang, X. Wang, X. Pu, J. Wang, C. Yan, Y. Cao, H. Yang, W. Li, X. Li, *Energy Environ. Mater.* **2022**. <https://doi.org/10.1002/eem2.12575>.
- [13] S. Islam, M. H. Alfaruqi, J. Song, S. Kim, D. T. Pham, J. Jo, S. Kim, V. Mathew, J. P. Baboo, Z. Xiu, J. Kim, *J. Energy Chem.* **2017**, *26*, 815–819.
- [14] S. Luo, L. Xie, F. Han, W. Wei, Y. Huang, H. Zhang, M. Zhu, O. G. Schmidt, L. Wang, *Adv. Funct. Mater.* **2019**, *29*, 1901336.
- [15] G. G. Yadav, J. W. Gallaway, D. E. Turney, M. Nyce, J. Huang, X. Wei, S. Banerjee, *Nat. Commun.* **2017**, *8*, 14424.
- [16] G.-T. Park, B. Namkoong, S.-B. Kim, J. Liu, C. S. Yoon, Y.-K. Sun, *Nat. Energy* **2022**, *7*, 946–954.
- [17] Z. Cui, X. Li, X. Bai, X. Ren, X. Ou, *Energy Storage Mater.* **2023**, *57*, 14–43.
- [18] Z. Wang, K. Han, Q. Wan, Y. Fang, X. Qu, P. Li, *ACS Appl. Mater. Interfaces* **2023**, *15*, 859–869.
- [19] X. Xia, Y. Zhao, M. Xu, W. Liu, X. Sun, *Nano Res.* **2023**, *16*, 2511–2518.
- [20] X. Ji, Y. Xu, H. Feng, P. Wang, Y. Zhou, J. Song, Q. Xia, Q. Tan, *ACS Appl. Mater. Interfaces* **2021**, *13*, 47659–47670.
- [21] G. Chen, Y. Cai, H. Zhang, D. Hong, S. Shao, C. Tu, Y. Chen, F. Wang, B. Chen, Y. Bai, X. Wang, Q. Dai, *Environ. Sci. Technol.* **2021**, *55*, 14204–14214.
- [22] Y. Zeng, J. Liang, J. Zheng, Z. Huang, X. Zhang, G. Zhu, Z. Wang, H. Liang, Y.-Z. Zhang, *Appl. Phys. Rev.* **2022**, *9*, 021304.
- [23] X. Niu, G. Zhu, Z. Yin, Z. Dai, X. Hou, J. Shao, W. Huang, Y. Zhang, X. Dong, *J. Mater. Chem. A* **2017**, *44*, 22939–22944.
- [24] N. Li, Z. Hou, S. Liang, Y. Cao, H. Liu, W. Hua, C. Wei, F. Kang, J.-G. Wang, *Chem. Eng. J.* **2023**, *452*, 139408.
- [25] Y. Li, X. Li, H. Duan, S. Xie, R. Dai, J. Rong, F. Kang, L. Dong, *Chem. Eng. J.* **2022**, *441*, 136008.

- [26] Y. Jiao, L. Kang, J. Berry-Gair, K. McColl, J. Li, H. Dong, H. Jiang, R. Wang, F. Cora, D. J. L. Brett, G. He, I. P. Parkin, *J. Mater. Chem. A* **2020**, *42*, 22075–22082.
- [27] N. Balke, S. Jesse, A. N. Morozovska, E. Eliseev, D. W. Chung, Y. Kim, L. Adamczyk, R. E. García, N. Dudney, S. V. Kalinin, *Nat. Nanotechnol.* **2010**, *5*, 749–754.
- [28] W. Xu, C. Sun, K. Zhao, X. Cheng, S. Rawal, Y. Xu, Y. Wang, *Energy Storage Mater.* **2019**, *16*, 527–534.
- [29] M. Wang, X. Wang, Z. Yao, W. Tang, X. Xia, C. Gu, J. Tu, *ACS Appl. Mater. Interfaces* **2019**, *11*, 24198–24204.
- [30] C. Wang, J. Zhang, X. Wang, C. Lin, X. S. Zhao, *Adv. Funct. Mater.* **2020**, *30*, 2002629.
- [31] W. Qiu, Y. Li, A. You, Z. Zhang, G. Li, X. Lu, Y. Tong, *J. Mater. Chem. A* **2017**, *28*, 14838–14846.
- [32] L. Chen, J. Jia, R. Ran, X. Song, *Chem. Eng. J.* **2019**, *369*, 1129–1137.
- [33] Y. Yuan, C. Liu, B. W. Byles, W. Yao, B. Song, M. Cheng, Z. Huang, K. Amine, E. Pomerantseva, R. Shahbazian-Yassar, J. Lu, *Joule* **2019**, *3*, 471–484.
- [34] C. Chen, M. Shi, Y. Zhao, C. Yang, L. Zhao, C. Yan, *Chem. Eng. J.* **2021**, *422*, 130375.
- [35] Q. Wang, W. Zhang, Z. Zhang, S. Liu, J. Wu, Y. Guan, A. Mei, Y. Rong, Y. Hu, H. Han, *Adv. Energy Mater.* **2020**, *10*, 1903092.
- [36] H.-Y. Lü, X.-H. Zhang, F. Wan, D.-S. Liu, C.-Y. Fan, H.-M. Xu, G. Wang, X.-L. Wu, *ACS Appl. Mater. Interfaces* **2017**, *9*, 12518–12527.
- [37] L. Zhang, C. Wang, Y. Liu, M. Ren, J. Du, A. Chen, F. Li, *Chem. Eng. J.* **2021**, *426*, 130813.
- [38] Y. Song, J. Li, R. Qiao, X. Dai, W. Jing, J. Song, Y. Chen, S. Guo, J. Sun, Q. Tan, Y. Liu, *Chem. Eng. J.* **2022**, *431*, 133387.
- [39] Y. Zhao, C. Chang, F. Teng, Y. Zhao, G. Chen, R. Shi, G. I. N. Waterhouse, W. Huang, T. Zhang, *Adv. Energy Mater.* **2017**, *7*, 1700005.
- [40] M. F. Fink, M. Weiss, R. Marschall, C. Roth, *J. Mater. Chem. A* **2022**, *29*, 15811–15838.
- [41] J. Lu, H. Wang, Y. Sun, X. Wang, X. Song, R. Wang, *Chem. Eng. J.* **2021**, *417*, 127894.
- [42] L. R. Pahalagedara, S. Dharmarathna, C. K. King'ondu, M. N. Pahalagedara, Y.-T. Meng, C.-H. Kuo, S. L. Suib, *J. Phys. Chem. C* **2014**, *118*, 20363–20373.
- [43] J.-G. Wang, D. Jin, R. Zhou, X. Li, X.-R. Liu, C. Shen, K. Xie, B. Li, F. Kang, B. Wei, *ACS Nano* **2016**, *10*, 6227–6234.
- [44] Y. Zhang, Y. Liu, Z. Liu, X. Wu, Y. Wen, H. Chen, X. Ni, G. Liu, J. Huang, S. Peng, *J. Energy Chem.* **2022**, *64*, 23–32.
- [45] W. Sun, F. Wang, S. Hou, C. Yang, X. Fan, Z. Ma, T. Gao, F. Han, R. Hu, M. Zhu, C. Wang, *J. Am. Chem. Soc.* **2017**, *139*, 9775–9778.
- [46] J. Huang, Z. Wang, M. Hou, X. Dong, Y. Liu, Y. Wang, Y. Xia, *Nat. Commun.* **2018**, *9*, 2906.
- [47] X. Zhang, S. Wu, S. Deng, W. Wu, Y. Zeng, X. Xia, G. Pan, Y. Tong, X. Lu, *Small Methods* **2019**, *3*, 1900525.
- [48] X. Li, Q. Zhou, Z. Yang, X. Zhou, D. Qiu, H. Qiu, X. Huang, Y. Yu, *Energy Environ. Mater.* **2022**, <https://dx.doi.org/10.1002/eem2.12378>.
- [49] Z. Wang, X. Yan, F. Wang, T. Xiong, M.-S. Balogun, J. Tang, H. Zhou, J. Deng, *Carbon* **2021**, *174*, 556–566.
- [50] L. Xu, Y. Xiao, Y. Yang, S.-J. Yang, X.-R. Chen, R. Xu, Y.-X. Yao, W.-L. Cai, C. Yan, J.-Q. Huang, Q. Zhang, *Angew. Chem. Int. Ed.* **2022**, *61*, e202210365.
- [51] R. B. Rakhi, W. Chen, D. Cha, H. N. Alshareef, *Nano Lett.* **2012**, *12*, 2559–2567.
- [52] J. Li, Y. Ding, S. Zhang, H. Li, B. Yin, T. Ma, *J. Power Sources* **2022**, *524*, 231074.
- [53] Q. Zhao, X. Chen, Z. Wang, L. Yang, R. Qin, J. Yang, Y. Song, S. Ding, M. Weng, W. Huang, J. Liu, W. Zhao, G. Qian, K. Yang, Y. Cui, H. Chen, F. Pan, *Small* **2019**, *15*, e1904545.
- [54] J. Wang, J.-G. Wang, H. Liu, C. Wei, F. Kang, *J. Mater. Chem. A* **2019**, *22*, 13727–13735.
- [55] J. Wang, J.-G. Wang, H. Liu, Z. You, Z. Li, F. Kang, B. Wei, *Adv. Funct. Mater.* **2021**, *31*, 2007397.
- [56] B. Yin, S. Zhang, K. Ke, W. S. V. Lee, Z. Wang, *ChemistrySelect* **2020**, *5*, 8951–8958.
- [57] X. Pu, D. Zhao, C. Fu, Z. Chen, S. Cao, C. Wang, Y. Cao, *Angew. Chem. Int. Ed.* **2021**, *60*, 21310–21318.
- [58] Y. Zhao, P. Zhang, J. Liang, X. Xia, L. Ren, L. Song, W. Liu, X. Sun, *Energy Storage Mater.* **2022**, *47*, 424–433.
- [59] D. Wu, L. M. Housel, S. T. King, Z. R. Mansley, N. Sadique, Y. Zhu, L. Ma, S. N. Ehrlich, H. Zhong, E. S. Takeuchi, A. C. Marschilok, D. C. Bock, L. Wang, K. J. Takeuchi, *J. Am. Chem. Soc.* **2022**, *144*, 23405–23420.
- [60] Y. Ma, M. Xu, R. Liu, H. Xiao, Y. Liu, X. Wang, Y. Huang, G. Yuan, *Energy Storage Mater.* **2022**, *48*, 212–222.
- [61] Q. Tan, X. Li, B. Zhang, X. Chen, Y. Tian, H. Wan, L. Zhang, L. Miao, C. Wang, Y. Gan, J. Jiang, Y. Wang, H. Wang, *Adv. Energy Mater.* **2020**, *10*, 2001050.
- [62] G. Kresse, J. Hafner, *Phys. Rev. B* **1993**, *47*, 558–561.
- [63] G. Kresse, J. Hafner, *Phys. Rev. B* **1994**, *49*, 14251–14269.
- [64] J. P. Perdew, K. Burke, M. Ernzerhof, *Phys. Rev. Lett.* **1996**, *77*, 3865–3868.
- [65] G. Kresse, D. Joubert, *Phys. Rev. B* **1999**, *59*, 1758–1775.
- [66] P. E. Blöchl, *Phys. Rev. B* **1994**, *50*, 17953–17979.

Manuscript received: March 30, 2023

Revised manuscript received: May 17, 2023

Accepted manuscript online: May 20, 2023

Version of record online: June 1, 2023